



Transparent and conductive electrodes by large-scale nano-structuring of noble metal thin-films

JES LINNET,^{1,2,*} ANDERS RUNGE WALTHER,^{3,4} CHRISTIAN WOLFF,¹
OLE ALBREKTSEN,^{3,5} N. ASGER MORTENSEN,^{1,6} AND JAKOB
KJELSTRUP-HANSEN²

¹Center for Nano Optics, Mads Clausen Institute, University of Southern Denmark, Campusvej 55, DK-5230 Odense M, Denmark

²NanoSYD, Mads Clausen Institute, University of Southern Denmark, Alsion 2, DK-6400 Sønderborg, Denmark

³The Mærsk Mc-Kinney Møller Institute, University of Southern Denmark, Campusvej 55, DK-5230 Odense M, Denmark

⁴Department of Chemical Engineering, Biotechnology and Environmental Technology, University of Southern Denmark, Campusvej 55, DK-5230 Odense, Denmark

⁵Electrical Engineering, Mads Clausen Institute, University of Southern Denmark, Campusvej 55, DK-5230 Odense M, Denmark

⁶Danish Institute for Advanced Study, University of Southern Denmark, Campusvej 55, DK-5230 Odense M, Denmark

*jeslinnet@gmail.com

Abstract: The widespread use of transparent conductive films in modern display and solar technologies calls for engineering solutions with tunable light transmission and electrical characteristics. Currently, considerable effort is put into the optimization of indium tin oxide, carbon nanotube-based, metal grid, and nano-wire thin-films. The indium and carbon films do not match the chemical stability nor the electrical performance of the noble metals, and many metal films are not uniform in material distribution leading to significant surface roughness and randomized transmission haze. We demonstrate solution-processed masks for physical vapor-deposited metal electrodes consisting of hexagonally ordered aperture arrays with scalable aperture-size and spacing in an otherwise homogeneous noble metal thin-film that may exhibit better electrical performance than carbon nanotube-based thin-films for equivalent optical transparency. The fabricated electrodes are characterized optically and electrically by measuring transmittance and sheet resistance. The presented methods yield large-scale reproducible results. Experimentally realized thin-films with very low sheet resistance, $R_{sh} = 2.01 \pm 0.14 \Omega/\text{sq}$, and transmittance, $T = 25.7 \pm 0.08 \%$, show good agreement with finite-element method simulations and an analytical model of sheet resistance in thin-films with ordered apertures support the experimental results and also serve to aid the design of highly transparent conductive films. A maximum Haacke number for these 33 nm thin-films, $\phi_H = 10.7 \times 10^{-3} \Omega^{-1}$ corresponding to $T \approx 80 \%$ and $R_{sh} \approx 10 \Omega/\text{sq}$, is extrapolated from the theoretical results. Increased transparency may be realizable using thinner metal films trading off conductivity. Nevertheless, the findings of this article indicate that colloidal lithographic patterned transparent conductive films can serve as vital components in technologies with a demand for transparent electrodes with low sheet resistance.

© 2018 Optical Society of America under the terms of the [OSA Open Access Publishing Agreement](#)

OCIS codes: (310.0310) Thin films; (310.7005) Transparent conductive coatings.

References and links

1. D. Hecht, L. Hu, and G. Irvin, "Emerging transparent electrodes based on thin films of carbon nanotubes, graphene, and metallic nanostructures," *Adv. Mater.* **23**(13), 1482–1513 (2011).

2. S. Oi, "Automotive Touch Panel Market Report," Tech. Rep. (2016). <https://goo.gl/3r7oyT>.
 3. G. Adiboina, "Thin Film Photovoltaic (PV) Cells Market Analysis to 2020," Tech. Rep. (2010). <https://goo.gl/v9ceGP>.
 4. J. Baljko, "Flexible Displays Poised for Explosive Growth," Tech. rep. (2013). <https://goo.gl/R5rnPb>.
 5. H. Hartnagel, *Semiconducting Transparent Thin Films* (Institute of Physics Publishing, 1995).
 6. VLSI Standards, *ITO Sheet Resistance Standard* (VLSI Standards, 2012).
 7. S. Kim, S. Choi, C. Park, and H. Jin, "Transparent conductive ITO thin films through the sol-gel process using metal salts," *Thin Solid Films* **347**(1), 155–160 (1999).
 8. H. Kim, A. Piqué, J. S. Horwitz, H. Mattoussi, H. Murata, Z. H. Kafafi, and D. B. Chrisey, "Indium tin oxide thin films for organic light-emitting devices," *Appl. Phys. Lett.* **74**(23), 3444–3446 (1999).
 9. S. Kirner, M. Hartig, L. Mazzarella, L. Korte, T. Frijnts, H. Scherg-Kurmes, S. Ring, B. Stannowski, B. Rech, and R. Schlattmann, "The Influence of ITO Dopant Density on J-V Characteristics of Silicon Heterojunction Solar Cells: Experiments and Simulations," *Energy Procedia* **77**, 725–732 (2015).
 10. A. G. Rinzler, J. Liu, H. Dai, P. Nikolaev, C. B. Huffman, F. Rodríguez-Macías, P. J. Boul, A. H. Lu, D. Heymann, D. T. Colbert, R. S. Lee, J. E. Fischer, A. M. Rao, P. C. Eklund, and R. E. Smalley, "Large-scale purification of single-wall carbon nanotubes: process, product, and characterization," *Appl. Phys. A Mater. Sci. Process.* **67**(1), 29–37 (1998).
 11. R. B. Pode, C. J. Lee, D. G. Moon, and J. I. Han, "Transparent conducting metal electrode for top emission organic light-emitting devices: Ca-Ag double layer," *Appl. Phys. Lett.* **84**(23), 4614–4616 (2004).
 12. J. Y. Lee, S. Connor, Y. Cui, and P. Peumans, "Solution-processed metal nanowire mesh transparent electrodes," *Nano Lett.* **8**(2), 689–692 (2008).
 13. W. He and C. Ye, "Flexible Transparent Conductive Films on the Basis of Ag Nanowires: Design and Applications: A Review," *J. Mater. Sci. Technol.* **31**(6), 581–588 (2015).
 14. K. Cheng, Z. Cui, Q. Li, S. Wang, and Z. Du, "Large-scale fabrication of a continuous gold network for use as a transparent conductive electrode in photo-electronic devices," *Nanotechnology* **23**, 42(2012).
 15. A. J. Morfa, E. M. Akinoglu, J. Subbiah, M. Giersig, and P. Mulvaney, "Transparent metal electrodes from ordered nanosphere arrays," *J. Appl. Phys.* **114**(5), 54502 (2013).
 16. T. Qiu, B. Luo, F. Ali, E. Jaatinen, L. Wang, and H. Wang, "Metallic nanomesh with disordered dual-size apertures as wide-viewing-angle transparent conductive electrode," *ACS Appl. Mater. Interfaces* **8**(35), 22768–22773 (2016).
 17. S. Baek, S. Ha, H. Lee, K. Kim, D. Kim, and J. Moon, "Monolithic Two-Dimensional Photonic Crystal Reflectors for the Fabrication of Highly Efficient and Highly Transparent Dye-Sensitized Solar Cells," *ACS Appl. Mater. Interfaces* **9**(42), 37006–37012 (2017).
 18. G. Haacke, "New figure of merit for transparent conductors," *J. Appl. Phys.* **47**(9), 4086–4089 (1976).
 19. T. M. Barnes, M. O. Reese, J. D. Bergeson, B. A. Larsen, J. L. Blackburn, M. C. Beard, J. Bult, and J. Van De Lagemaat, "Comparing the fundamental physics and device performance of transparent, conductive nanostructured networks with conventional transparent conducting oxides," *Adv. Energy Mater.* **2**(3), 353–360 (2012).
 20. American Society for Testing and Materials, *Annual book of ASTM standards* (American Society for Testing and Materials, 1975).
 21. I. Miccoli, F. Edler, H. Pfnür, and C. Tegenkamp, "The 100th anniversary of the four-point probe technique: the role of probe geometries in isotropic and anisotropic systems," *J. Phys. Condens. Matter* **27**(22), 223201 (2015).
 22. F. M. Smits, "Measurement of Sheet Resistivities with the Four-Point Probe," *Bell Syst. Tech. J.* **37**(3), 711–718 (1958).
 23. W. Zhang, S. H. Brongersma, O. Richard, B. Brijis, R. Palmans, L. Froyen, and K. Maex, "Influence of the electron mean free path on the resistivity of thin metal films," *Microelectron. Eng.* **76**(1), 146–152 (2004).
 24. A. Plettl, F. Enderle, M. Saitner, A. Manzke, C. Pfahler, S. Wiedemann, and P. Ziemann, "Non-Close-Packed crystals from self-assembled polystyrene spheres by isotropic plasma etching: adding flexibility to colloid lithography," *Adv. Funct. Mater.* **19**(20), 3279–3284 (2009).
 25. E. Devaux, T. Ebbesen, J. C. Weeber, and A. Dereux, "Launching and decoupling surface plasmons via micro-gratings," *Appl. Phys. Lett.* **83**(24), 4936–4938 (2003).
 26. A. Bouhelier, T. Huser, H. Tamaru, H.-J. Güntherodt, D. W. Pohl, F. I. Baida, and D. Van Labeke, "Plasmon optics of structured silver films," *Phys. Rev. B* **63**(15), 155404 (2001).
 27. A. Zayats, I. I. Smolyaninov, and A. A. Maradudin, "Nano-optics of surface plasmon polaritons," *Phys. Rep.* **408**(3-4), 131–314 (2005).
 28. D. L. Mills, "Attenuation of surface polaritons by surface roughness," *Phys. Rev. B* **12**(10), 4036–4046 (1975).
 29. Y. Peng, T. Paudel, W. C. Chen, W. J. Padilla, Z. F. Ren, and K. Kempa, "Percolation and polaritonic effects in periodic planar nanostructures evolving from holes to islands," *Appl. Phys. Lett.* **97**(4), 2–4 (2010).
 30. Z. Li, H. Kandel, E. Dervishi, V. Saini, A. Biris, A. Biris, and D. Lupu, "Does the wall number of carbon nanotubes matter as conductive transparent material?" *Appl. Phys. Lett.* **91**(5), 053115 (2007).
 31. L. Malaquin, T. Kraus, H. Schmid, E. Delamarche, and H. Wolf, "Controlled particle placement through convective and capillary assembly," *Langmuir* **23**(23), 11513–11521 (2007).
 32. COMSOL AB, "COMSOL MultiPhysics Reference Manual, version 5.3," COMSOL, Inc, www.comsol.com (2017).
 33. P. B. Johnson and R. W. Christy, "Optical constants of the noble metals," *Phys. Rev. B* **6**(12), 4370–4379 (1972).
 34. I. H. Malitson, "Interspecimen Comparison of the Refractive Index of Fused Silica," *J. Opt. Soc. Am.* **55**(10), 1205 (1965).
-

1. Introduction

Many modern devices feature transparent conductive films (TCFs) as essential elements to their performance. The use of TCF is extensive in technologies such as touch panels, smartphones, organic light-emitting diodes, and liquid crystal displays (LCDs). While the LCD technology by far is the largest user of transparent conductive materials [1], many devices utilizing transparent electrodes currently experience incredible growth - production of automotive touch panels [2] and thin-film photovoltaics [3] more than doubled since 2013, and emerging flexible display market trends promise up to \$40 Billion growth in only seven years, from 2013–2020 [4].

A widely used material for TCFs is indium tin oxide (ITO), an n-type degenerate, 3.7 eV optical band-gap semiconductor [5]. It is transparent in the visible spectral region and reflective in the infrared. ITO can achieve relatively low electrical resistivity, $\sim 15 \text{ Ohms per square } (\Omega/\text{sq})$ sheet resistance [6], making it a good transparent conductive material for various electronic applications. However, ITO does not come without shortcomings: high performance films require high deposition vacuum (although compatible with the sol-gel method [7], this yields more resistive coatings $\sim 10^3 \text{ } \Omega/\text{sq}$), ITO also requires high deposition or annealing temperature [8], it is brittle by nature and the limited global supply has begun to drive research into alternative TCFs [1]. Thin films of ITO must be processed carefully and methodically in order to achieve reproducible performance which varies with doping concentration [9], crystal orientation, and surface roughness. Consequently, ITO is a challenging candidate for transparent electrodes in touch screens and flexible electronics. Alternatively, more elastic carbon nanotube-based thin films [10] can be used at the cost of significantly increased sheet resistance ($\sim 200 \text{ } \Omega/\text{sq}$). Touch screens, for example, need sheet resistance in the range of $50\text{--}300 \text{ } \Omega/\text{sq}$, whereas, sheet resistance as small as $10 \text{ } \Omega/\text{sq}$ is required for applications in solar cell electrodes, organic light emitting diode displays and LCDs [1].

Previously, patterned metal grids and nano-wires of Ag have been used as noble metal TCFs. In metal grids [11], the advantage lies in the complete transparency in between grid lines, but this comes with a greatly increased sheet resistance in the periodically discontinuous sheet which can only be compensated by creating thicker grid lines at the price of significant surface roughness. The randomly arranged Ag nano-wire approach has shown very promising results with low sheet resistance and high transmittance [12]. This technique yields a random grid of nano-wires in which uniformity is improved compared to the metal grid, however, it opens up the possibility of structural damage by electromigration of Ag ions in response to an applied current [1]. The significant diameter ($50\text{--}200 \text{ nm}$) of the oftentimes stacked Ag nano-wires increases surface roughness, which combined with the randomized wire length and spacing as well as the required annealing process results in transmission haze, i.e. uneven light scattering, which is undesirable in most display applications, but can be advantageous in solar cells. Nevertheless, nano-wire TCFs show great promise for cheap, large-scale manufacturing of highly transparent and conductive electrodes. An extensive review provides more details on nano-wire TCFs [13].

Polystyrene particles (PSP) have previously been used as masks for TCFs [14–17] showing promising experimental results, e.g. a way to minimize the iridescence of these films by employing polydisperse particles [16] and a way to engineer highly efficient and wavelength-selective reflectors [17]. Theoretically, however, in those works transmission is either solely experimentally determined or estimated by a simple geometric model not considering surface plasmon absorption and no theoretical analysis is presented for the TCF sheet resistance.

In the present work, we investigate the PSP nanofabrication method (PSP method) which facilitates large-scale nano-structuring of physical vapor-deposited (PVD) thin-films utilizing a spin-coated monolayer of PSP as a mask, in fabrication of hexagonally ordered nano-apertures, yielding an electrically conductive and optically transparent film.

The fabrication details and experimental results on optical transmission and electrical sheet resistance are documented in this paper and supported by (1) an analytical resistance model

based on the nano-structured geometry and (2) time-harmonic finite-element simulations of the electric field using a commercially available finite-element method (COMSOL MultiPhysics). The Haacke figure-of-merit [18], which has been shown to correlate well with current losses in photovoltaics [19], is used for evaluating the electro-optical performance of the TCF.

2. Experimental section

Experimentally, full wafer coverage of a mono-layer of PSP was achieved by the following procedure. (1) A 0.5 mm thick 4" BK7 SiO₂ wafer (PSP wafer) was rinsed sequentially in a 3:1 mixture of sulfuric acid and hydrogen peroxide solution for 60 s, ethanol, and deionized water and followed by drying with nitrogen gas. (2) An aqueous solution containing 10 wt.-% PSP of diameter $d_0 = 1.05 \pm 0.03 \mu\text{m}$ (purchased from Microparticles GmbH) was mixed 1:1 with ethanol to a total volume of 400 μL and spin-coated on the rinsed wafer using a RRT Lanz EBS11 spin-coater configured for three spin steps: 200 RPM for 15 s, 485 RPM for 60 s and 6000 RPM for 10 s.

The individual size of the PSPs in the mono-layer was reduced using ICP-RIE by mounting the PSP wafer on an Si carrier wafer with wafer grease (Apiezon "H" Grease). This was done to achieve sufficient cooling at the wafer-PSP interface during etching in order to minimize any movement of the PSPs during ICP-RIE. Etching was performed in an Alcatel AMS110 SE ICP-RIE system using an oxygen flow of 200 sccm and an RF power of 1000W for 190 s at -20°C . Subsequently the wafers were separated using a thin pry tool and the remaining wafer grease on the PSP wafer back-side was removed using acetone and isopropanol wetted cleanroom cloths.

Ag thin-films (30 nm at 1.0 $\text{\AA}/\text{s}$) with a Ti adhesion layer (3 nm at 0.2 $\text{\AA}/\text{s}$) were deposited by electron-beam evaporation using a Polyteknik Cryofox Explorer 600 LT. Lift-off (dissolving PSPs) was carried out using a Struers Heidolph POLYMAX 2040 waving platform shaker 24 h at 12 rev/min shaking a mounted petri dish containing acetone heated to $\sim 30^\circ\text{C}$ by an incandescent lamp, followed by 30 min sonication in acetone at $\sim 45^\circ\text{C}$, 15 min sonication in isopropanol at room temperature, rinsing in deionized water and finally blown dry with nitrogen gas.

The sheet resistance, $R_{\text{sh}} = \rho/t$ where ρ is the resistivity and t is the film thickness of the nano-structured TCF, was measured using the four-point probe technique which is an established method in the microelectronics industry as a reference procedure for resistivity measurements [20]. This probe technique uses four electrodes equally spaced with spacing s and oriented along a straight line. In the experiment a Keithley 2400 SourceMeter and a LUCAS LABS S-302-4 Resistivity Test Stand with four-point in-lines probes ($s = 1.016 \text{ mm}$) are used to pass a current (I) through the two outermost electrodes and measure the voltage drop (V) across the two innermost electrodes. For an infinite 2D sheet, with length, width, and thickness, $\{l, w\} \gg s \gg t$, the current density can be assumed to spread cylindrically from the first electrode and the resistivity can be derived as [21]: $\rho_{2D} = (\pi t / \ln 2)(V/I)$. However, in the present case the Ag thin-film is deposited in a square pattern ($l = w$) with $l/s = 20$, and the prefactor, $P = \pi / \ln 2$ for an infinite film, is consequently changed to 4.45 [22]. The measured sheet resistance is determined as $R_{\text{sh}} = P(V/I)$ and the measured conductivity is determined as $\sigma_{\text{sh}} = (R_{\text{sh}}t)^{-1}$.

Optical transmittance was measured using an integrating sphere configuration of a PerkinElmer Lambda900 spectrophotometer. Spectral characterization of transmittance $T = I_{\text{TCF}}/I_0$ was carried out on nano-perforated TCF (I_{TCF}) relative to a blank (no sample inserted, I_0) measurement with a spectral resolution of 2 nm from 300–800 nm.

The electrical and optical performance of the nano-structured TCF was theoretically evaluated using a commercially available finite-element solver (COMSOL MultiPhysics) to solve an electrical current conservation equation based on Ohm's law and a time-harmonic wave equation for the optically transmitted electric field distribution (see Supporting Information).

The Haacke number, used for comparing the performance of TCFs, is defined as [18]:

$$\phi_H = T^{\mathcal{H}}/R_{\text{sh}} [10^{-3}\Omega^{-1}], \quad (1)$$

where $\mathcal{H} = 10$ in the figure of merit proposed by Haacke, and transmittance (T) is taken as an average value in the 400–700 nm wavelength range.

3. Results and discussion

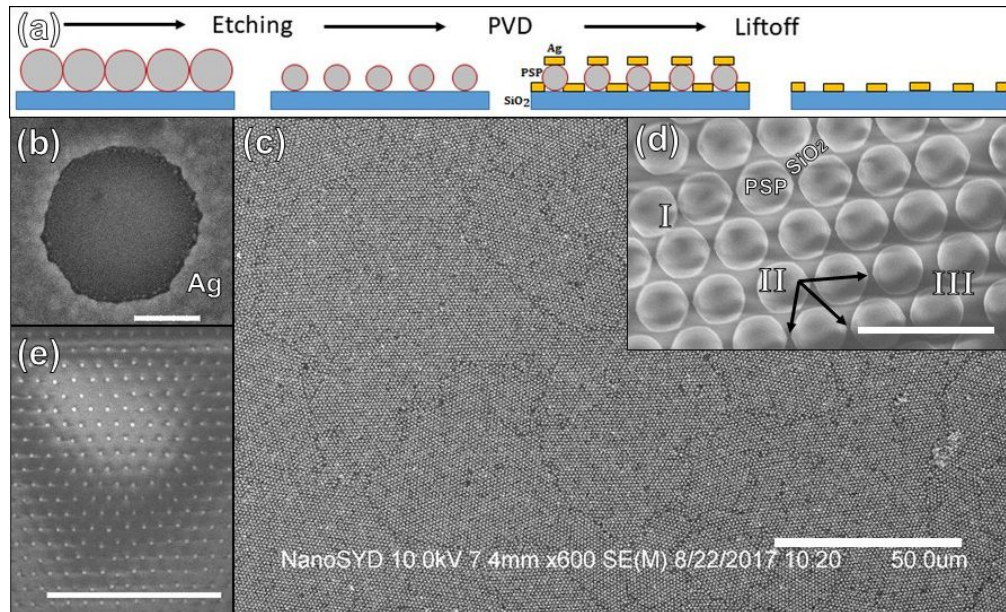


Fig. 1. (a) Schematic illustration of the fabrication process. (b) A single nano-aperture after Ag PVD. Scale bar: 200 nm. (c) Low magnification micrograph of deposited Ti+Ag (3+30 nm) thin-film on homogenous PSP monolayer demonstrating large-scale feasibility. Scale bar: 50 μm. (d) PSP monolayer on an SiO₂ substrate after spin-coating and a short (60 s) ICP-RIE sequence: Contacting PSP result in disconnected veins, I. The PSP edge closest to neighbor particles show bridge-forming tendency which thins the veins, II. Large gaps result in thicker inter-aperture veins, III. Scale bar: 2 μm. (e) PSP monolayer after spin-coating and a long (3 min) ICP-RIE sequence resulting in $d = 206.7 \pm 1.7$ nm, $d/d_0 = 0.197$ demonstrating that original PSP positions are preserved even for significant size reduction. Scale bar: 10 μm.

In the fabrication process the diameter of the PSPs is reduced by ICP-RIE prior to Ag PVD and a subsequent lift-off process, Fig. 1(a), and an electron micrograph of a single nano-aperture after lift-off indicates that almost circular apertures are realized and also that several small Ag nano-particles with diameters below 20 nm reside on the SiO₂ substrate near the aperture edges, Fig. 1(b). The deposited Ti+Ag (3+30 nm) thin-film on a homogeneous PSP monolayer demonstrates the large-scale feasibility of the PSP method, Fig. 1(c). The result of a short 60 s ICP-RIE sequence reveals (1) PSPs contact neighboring particles at various points [Fig. 1(d), I], disconnecting some of the veins after Ag PVD and decreasing conductivity locally, (2) a tendency for neighboring particles to form bridges for very short etch durations which causes a thinning of the veins [Fig. 1(d), II], i.e. decreasing the conductivity, and (3) large inter-particle gaps [Fig. 1(d), III], which decreases transmission while increasing conductivity due to the larger inter-particle Ag veins after PVD. The homogeneity of the PSP monolayer and the subsequent metal coating is thus influenced by the ICP-RIE sequence (see Supporting Information for additional

micrographs displaying domain homogeneity before and after the ICP-RIE sequence, Fig. S1, S2). Finally, Fig. 1(e) shows that it is possible to preserve periodicity even after significant reduction in PSP diameters (here, $d = 206.7 \pm 1.7$ nm so that $d/d_0 = 0.197$). Electron micrographs in Fig. 1(d,e) indicate dielectric charging in the insulating (PSPs on SiO₂) samples. In micrograph (c) the TCF was electrically grounded to the SEM stage.

In Fig. 2, the ratio between the bulk conductivity, σ_B , and the TCF sheet conductivity, σ_{sh} , is plotted as a function of the ratio between the aperture diameter, d , and the initial PSP diameter d_0 , using ab-initio finite-element simulations (see Supporting Information), a geometrical-, and an analytical resistance model. Bulk conductivity of materials cannot be experimentally achieved in thin-films when film thicknesses are comparable to the electron mean free path [23], therefore, in the measured data, σ_B is taken as the measured sheet conductivity of a thin-film without nano-patterned apertures. The geometrical model is an integration of infinitesimal area elements using the resistivity of Ag and the area of each element encountered when integrating from the current source to ground along a straight line. For conductivity simulation details see Supporting Information. The analytical resistance model is developed for the limit of large apertures (see Supporting Information) and provided here to aid the design of high-transparency conductive films:

$$\frac{\sigma_B}{\sigma_{sh}} = \frac{2\sqrt{3}}{\sqrt{a^2 - 2a}} \arctan\left(\frac{2-a}{\sqrt{a^2 - 2a}} \tan \frac{\pi}{12}\right), \quad (2)$$

where σ_B , $\sigma_{sh} = \frac{1}{R_{sh}}$ is the bulk and sheet conductivity, respectively and $a = \ln(d/d_0)$.

The measured sheet resistance values are reproducible from wafer to wafer as shown by the 0.8 σ_{sh}/σ_B double measurement point. Some measurement points show better conductivity than the models indicate, which is caused by imperfect packing of the PSP. The hexagonal packing occurs in domains which have boundaries and imperfections. The mean size of these domains is estimated from electron micrographs: $1200 \pm 700 \mu\text{m}^2$. Any slip in the grid of PSPs prior to PVD results in higher metal coverage at the cost of transmittance. This effect is, at these measurement points, believed to dominate over the tendency for veins to disconnect due to contacting PSP and for veins to thin as a result of the bridge-forming phenomena. For the limit of large apertures, however, the measured sheet resistance is lower than model predictions. This is likely caused by the experimental aperture-size limit dictated by neighboring particles forming bridges (which will disconnect the veins in the subsequent PVD) during very short etch procedures due to reduced accessibility of the oxygen plasma in the space between neighboring PSPs. Adding a voltage bias and grounding the wafer chuck during ICP-RIE generates a more anisotropic plasma with relatively improved oxygen plasma access to the mentioned bridges [24] possibly providing means for engineering a solution to avoid the disconnections. The simulated conductivity is considered the most accurate predictor for a fabrication-optimized specimen over the entire d/d_0 range, as the simulation considers conductivity in an ideal geometry. The analytical resistance model agrees with the simulations for the limit of large apertures (inset, Fig. 2).

In Fig. 3, we compare the measured and simulated optical transmittance of the 33 nm thin TCFs as a function of wavelength for various aperture-sizes and their simulation-calculated TCF sheet resistance. The measured transmittance of the TCF is seen to agree well with the simulation, and it is, at some wavelengths, higher and at others lower than the theoretical prediction (inset, Fig. 3). For this specimen, the measured average transmittance is $T = 25.7 \pm 0.08\%$ in the wavelength range 400–700 nm and the measured sheet resistance is $R_{sh} = 2.01 \pm 0.14 \Omega/\text{sq}$ which corresponds to a conductivity ratio of $\sigma_{sh}/\sigma_B \approx 0.8$ (Fig. 2). Near-field studies have demonstrated that hole arrays can be used to locally scatter surface plasmons into free-space light propagation through a non-trivial decoupling mechanism [25], which may explain the increase in the measured transmittance compared to the finite-element method calculated values in the

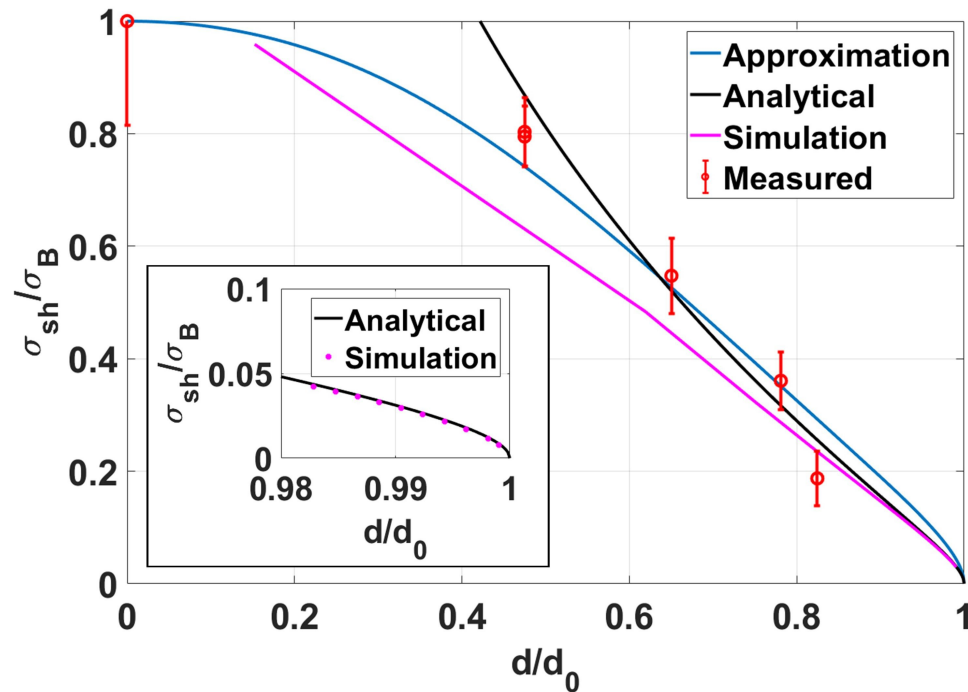


Fig. 2. Ratio between bulk conductivity (σ_B) and TCF sheet conductivity (σ_{sh}) as a function of the aperture and initial particle diameter ratio. Blue: Geometrical model. Black: Analytical resistance model for the limit of large apertures. Purple: Finite-element model calculation of unit-cell resistance. Red: Conductivity measured on fully TCF-covered wafers. Inset shows that the analytical resistance model predicts the same results as the simulation in the limit of large apertures.

short wavelength range in the visible spectrum (inset, Fig. 3). The measured transmittance may also be higher due to the non-atomically flat and non-ideally ordered Ag films. The metal film surface and aperture edge roughness and imperfect aperture ordering introduces discontinuities such as ridges, pits or abrupt changes in the interface where propagating plasmons may decouple and radiate into free-space light propagation [26, 27], rather than continue propagation until fully dissipated in the metal film [28]. Transmittance may be reduced by two effects. First, due to partial lift-off of PSP and Ag which may leave trace materials on the SiO_2 surface inside the transmitting apertures. Secondly, previously mentioned PSP grid imperfections resulting in thicker inter-aperture veins.

Generally, the measured transmittance of the TCFs agrees with the simulated results. The measurement contains fewer spectral features (inset, Fig. 3), likely due to the experimentally imperfect hexagonal ordering of nano-apertures in the Ag film array interrupting periodicity. The average transmittance over the wavelength range 400–700 nm tends to saturate towards $T \approx 80\%$ for a linearly increasing sheet resistance.

In the literature, the Haacke number is used for relative comparison of TCF performance. When using this figure of merit, transmission should be theoretically estimated including loss effects. Theoretical models based on geometrical optics to evaluate the transmission tend to overestimate the transmission by neglecting loss effects [15]. These models are most inaccurate for nano-patterned films, as plasmonic field confinement effects tend to increase loss and evidently decrease transmission. The transmittance simulated in Fig. 3 includes the dissipation effects in the

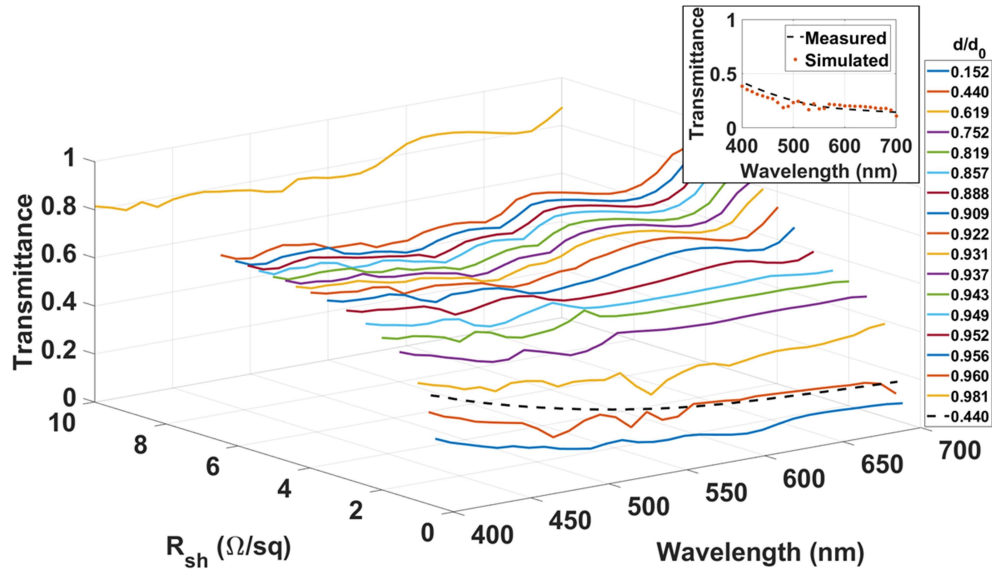


Fig. 3. Simulated (continuous) and measured (dashed) optical transmittance in the visible wavelength range (400–700 nm) for a selection of TCFs with $< 10 \Omega/\text{sq}$ simulated sheet resistance. Inset: Calculated data points (dotted) and measured (dashed) transmittance for the $d/d_0 = 0.44$ specimen.

flat metal by using the complex refractive index and even for the largest fill factor ($d/d_0 = 0.981$, $d = 1030 \text{ nm}$ which leaves only $w = 20 \text{ nm}$ vein width) transmittance averages to $79.8\% \pm 3.7\%$ in the wavelength range 400–700 nm which is significantly lower than predicted by a simple geometrical model [15]:

$$T \approx \frac{\pi(d_0/2 - w/2)^2}{2\sqrt{3}(d_0/2)^2} \approx 0.873, \quad (3)$$

where $w = d - d_0$. The tendency of lower transmission compared to the geometrically predicted value is likely due to plasmon absorption [29]. When approaching the limit of $d/d_0 \rightarrow 1$, the thin-film resistivity diverges while the transmittance has finite converged values suggesting that there is a theoretical limit to the highest achievable Haacke number in TCF's fabricated with the PSP method.

Given proper experimental TCF fabrication optimization the PSP method can, for the investigated $3 + 30 \text{ nm}$ Ti+Ag film, yield $\sim 80\%$ average transmittance in the 400–700 nm range while keeping a simulation-calculated sheet resistance $\leq 10 \Omega/\text{sq}$, which corresponds to a Haacke number of $10.7 \times 10^{-3} \Omega^{-1}$. In comparison, carbon nanotube-based thin-films have sheet resistance of 100–400 Ω/sq at $T \approx 80\%$ [30] so the proposed TCF may exhibit better electrical performance at equivalent optical transparency. The transparency and sheet conductance of TCFs fabricated with other methods and materials have been compared in review [1]. Further, the deposited film thickness essentially defines the surface roughness of the fabricated TCF and the initial wafer-size dictates the TCF size-limit.

In outlook, significantly higher Haacke numbers may be achieved by utilizing thinner Ag films, which would lower conductivity for a higher transmission due to the penetration depth of incident light. A few second hotplate treatment prior to ICP-RIE [15] may be preferable to freezing temperatures during ICP-RIE, as PSP tend to melt at the interface and better stick to their

initial positions, resulting in better periodicity after etching - this change may, however, make it harder to remove residual polystyrene on the SiO₂ surface inside the nano-apertures during the lift-off process. Fabricating a monolayer of PSP with spin-coating can be optimized by tailoring of the recipe or using adhesive coatings such as hexamethyldisilazane (HMDS). Rather than spin-coating, convective assembly of a particle suspension in a liquid may yield better results in even larger areas [31]. Convective assembly of PSP for noble metal TCF fabrication comes with the added benefit that it can straightforwardly be realized on flexible, non-wafer substrates.

In terms of fabrication cost, the PSP method employed here uses relatively expensive monodisperse PSP to define a mask for a high vacuum physical vapor deposition of the Ag thin-film. Both the initial particle cost for the mask and PVD requisites should be considered with regard to a cost-performance trade-off. In comparison to Ag nanowires, the PSP method provides better performance in terms of surface roughness, film homogeneity and reduced transmission haze. It should be mentioned that the vacuum processing steps used in our approach makes it more expensive, however, these techniques are nonetheless industry standard methods and can thus be scaled up to reduce processing cost. We postulate the fabrication cost can be reduced further by employing cheaper polydisperse particle solutions with the added benefit that the randomized particle size and thus aperture size tends to reduce iridescence of the fabricated films [16]. We further postulate that the PSP hotplate treatment, rather than cooling during etching, may sufficiently stick the PSP to the substrate so that relatively cheap barrel ashing can substitute ICP-RIE. Finally, relatively inexpensive Al could be utilized instead of Ag for the coatings.

4. Conclusion

The proposed fabrication method offers an engineering solution to transparent conductive films with a tunable tradeoff between optical transmission and electrical sheet resistance that should be able to satisfy performance requirements for widely different applications. In this work, transparent conductive films have been realized on 100 mm wafer-sized samples demonstrating the large-scale feasibility of the experimental methods. Generally, transparent conductive films fabricated using the polystyrene particle method have low sheet resistance, low chemical reactivity, high ductility, low surface roughness relative to other noble metal solutions and transmission of the transparent conductive films is ultimately limited by plasmonic losses. The simulations indicate that, in the limit of large apertures, transmission tends to converge and as an estimate $\sim 80\%$ transmittance can be achieved while keeping sheet resistance $\leq 10 \Omega/\text{sq}$. Further increase of the aperture size causes the sheet resistance to diverge rapidly to high values, suggesting that there is a theoretical maximum Haacke number ($10.7 \times 10^{-3} \Omega^{-1}$ for $t = 33 \text{ nm}$) that can be achieved for each thin-film thickness with this method. Reduced thin-film thickness will yield increased transparency at the cost of conductivity which may yield even higher Haacke numbers. An analytical model predicting the sheet resistance in the limit of large apertures has been developed, and it can assist in the design of transparent conductive films fabricated by the polystyrene particle method. The models and measurements confirm each other's predictions in both conductivity and transmission. Experimentally, the achieved uniformity of polystyrene particle distribution affect the efficiency of the resulting transparent conductive electrode. Spin-coating polystyrene particles did not result in perfect ordering. Inter-aperture discontinuities are present causing size variations in the conducting veins and influencing the overall periodicity which seem to, in measurement, smooth out the transmittance spectrum and affect the sheet resistance, so that experimentally realized films turned out to be more conductive at low d/d_0 ratios and less conductive at high d/d_0 ratios compared to model predictions. The findings of this article indicate that colloidal lithographic-patterned transparent conductive films can serve as vital components in technologies with a demand for transparent electrodes with low sheet resistance and may prove to be a promising candidate for electrodes in flexible solar-cells. The

advantage of this method lies in the low surface roughness and periodicity of the resulting film, which limits the randomized transmission haze relative to other noble metal-structured films.

5. Appendix

This supporting information contains additional micrograph data, elaborates on the transmission calculations based on the finite-element method simulations that were carried out using a commercially available software package (COMSOL MultiPhysics) and also gives an account of the applied analytical model calculation of the sheet resistance.

5.1. Additional micrograph data

Presented here (Fig. 4, 5) are additional electron micrographs of the PSP monolayer before the ICP-RIE sequence and the deposited Ti+Ag (3 + 30 nm) thin-film on a homogeneous PSP monolayer after the ICP-RIE sequence, respectively, illustrating the influence of the ICP-RIE sequence and the homogeneity and size of the hexagonally close-packed domains making up the transparent conductive film. The estimated mean size of the domains is $1200 \pm 700 \mu\text{m}^2$.

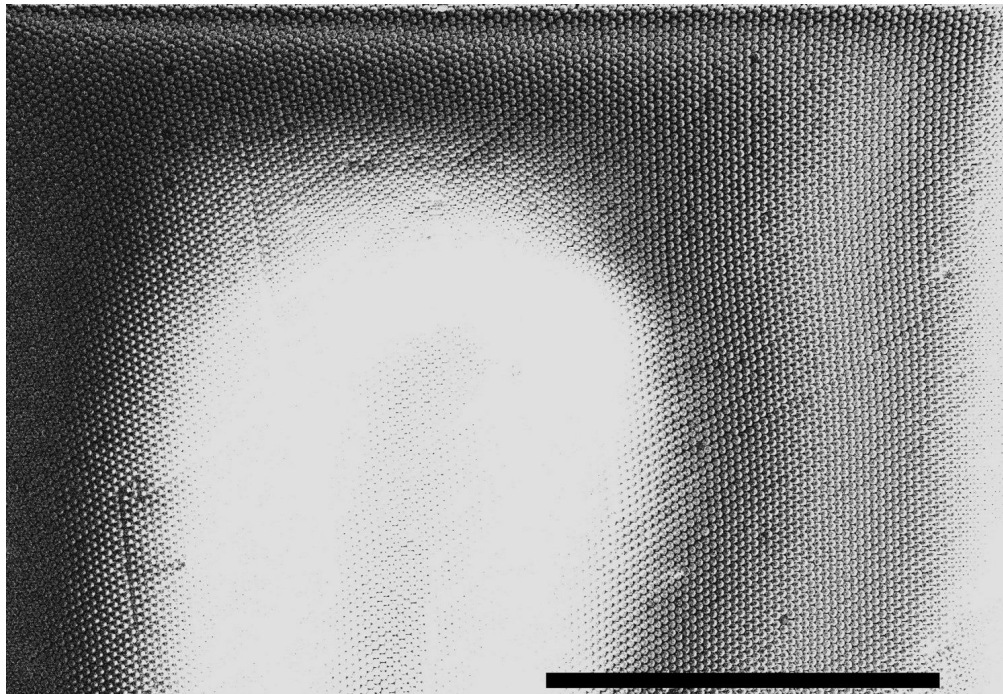


Fig. 4. Scanning electron micrograph of spin-coated PSP prior to the size-reducing ICP-RIE sequence. Scale bar $40 \mu\text{m}$.

5.2. Details on finite-element calculations

The geometry of the aperture grating is, for the optical transmittance simulation, represented by an infinite array of hexagonal unit cells consisting of an Ag film with one cylindrical aperture on an SiO_2 layer (Fig. 6). Materials are defined by the complex refractive index of Ag, SiO_2 and unity for the air volume. The array is defined by continuous periodic boundary conditions (PC) on each pair of opposite vertical surfaces and the unit-cell is end-capped by perfectly matched layers (PML). The port emits a linearly polarized electric field at the simulated wavelength with

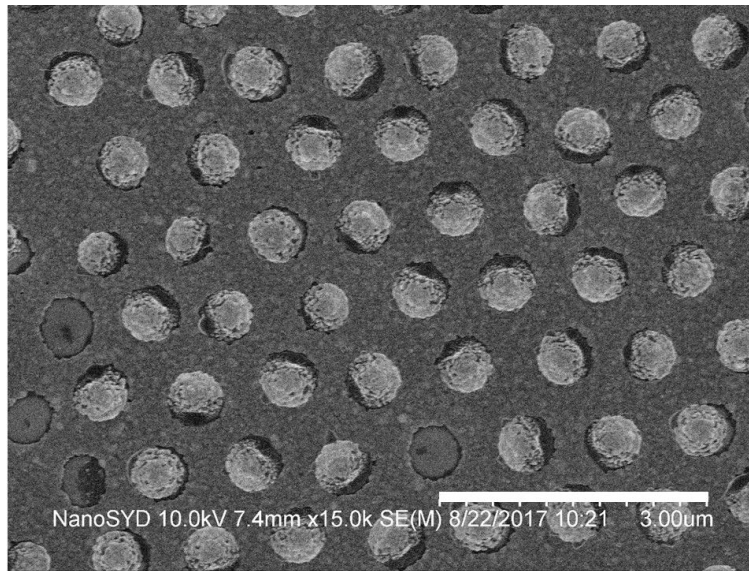


Fig. 5. Scanning electron micrograph of a physical vapour deposited Ti+Ag (3 + 30 nm) thin-film on a monodomain of ICP-RIE sequenced PSP. Scale bar 3 μm .

power flow direction indicated by the red arrow (Fig. 7). The software solves the time-harmonic wave equation for the electric field [32]:

$$\nabla \times \nabla \times \vec{E} - \left(\frac{\omega}{c}\right)^2 \left(\epsilon_r - \frac{i\sigma}{\omega\epsilon_0}\right) \vec{E} = 0, \quad (4)$$

where \vec{E} is the electric field, ϵ_0 , ϵ_r the vacuum and relative permittivity, respectively, c the speed of light in vacuum, ω the angular frequency, and σ is the conductivity. Materials are defined using optical constants from the literature: Ag by Johnson & Christy [33] and SiO_2 by Malitson [34].

The transmittance is calculated by the wave optics module in the visible spectrum ($\lambda = 400\text{--}700$ nm, in steps of 10 nm) for the selected aperture sizes (d) utilizing simulation-calculated scattering parameters including all allowed orders of transmitted diffraction. The transmittance simulation was carried out using the ABACUS 2.0 supercomputer at the DeIC National HPC Centre, University of Southern Denmark.

For the DC-conductivity calculation the evaluation time scale is very long compared to the charge relaxation time, enabling calculation of the stationary solution to the equation of continuity. The COMSOL 'Electric Currents' interface used for conductivity simulations solves the stationary field equations; a slightly more general form of Ohm's law [32]. Sheet resistance was calculated using an infinite sequence of rectangular unit cells of Ag thin-films containing apertures defined by ground and a current source planes in x-z planes and periodic boundary conditions (PC) on the y-z planes (Fig. 8). The current source delivers 1 A and the corresponding voltage drop is calculated by the finite element modeling software and used to calculate R_{sh} for select values of aperture diameters, d .

5.3. Details on analytical resistance model

The analytical resistance model is applicable in the limit of large apertures, i.e. when most of the voltage drop occurs across the thin veins between two apertures and when the voltage distribution

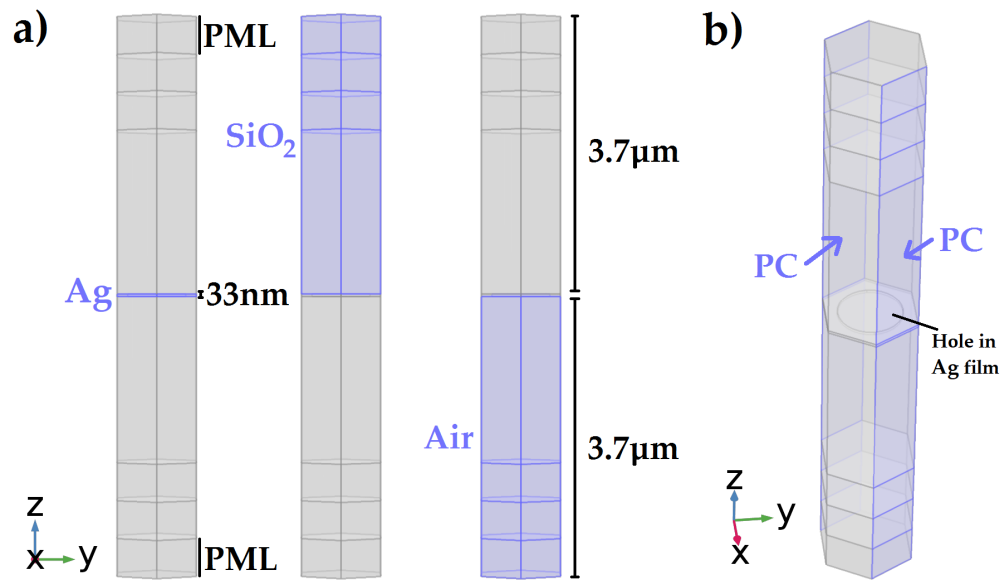


Fig. 6. Air, aperture grating in Ag film on glass substrate unit cell geometry for numerical simulation of transmittance. a) side view with material domains and b) slightly tilted view to reveal aperture in film and exemplifying periodic boundary conditions (PC).

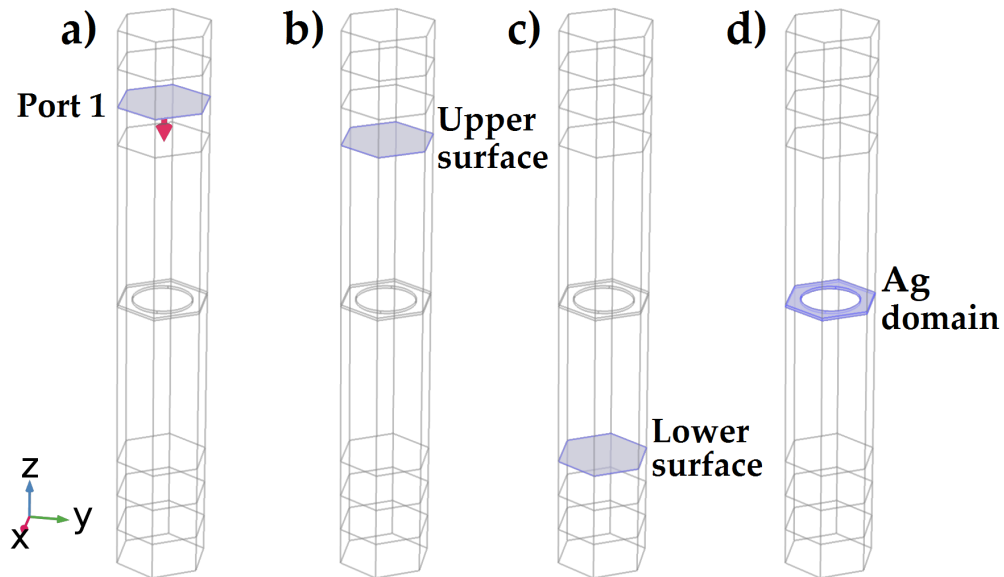


Fig. 7. Aperture grating in Ag film on glass substrate unit cell; a) Periodic port wave excitation surface (arrow indicates power flow direction), b), c) Upper and lower hypothetical surface for power flow calculations and d) Ag volume representing the unit cell of the investigated TCF.

in the thick nodes between three apertures is less relevant. As a result, we approximate the film as a network of resistors, each representing one vein, as illustrated in Fig. 9.

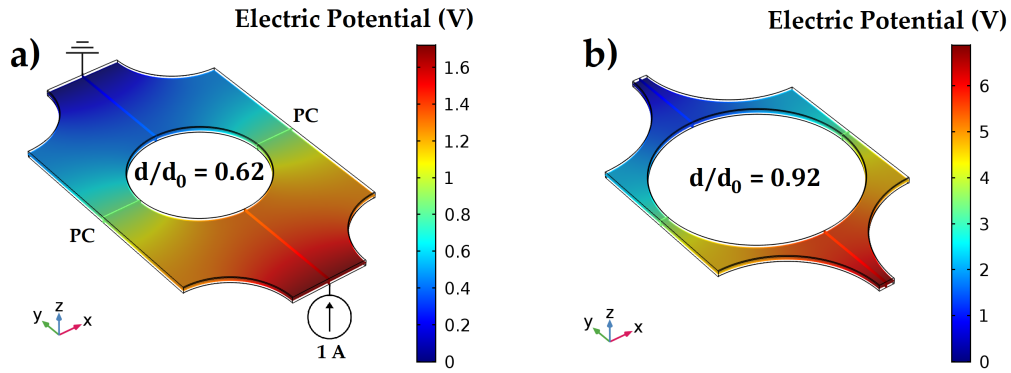


Fig. 8. Example rectangular Ag film unit cells containing apertures with side wall boundary conditions: 1 A current source, ground and periodic boundary conditions (PC) used for sheet resistance simulation. $d_0 = 1050$ nm, a) $d = 650$ nm and b) $d = 968$ nm apertures. The calculated change in electric potential is used to calculate the sheet resistance.

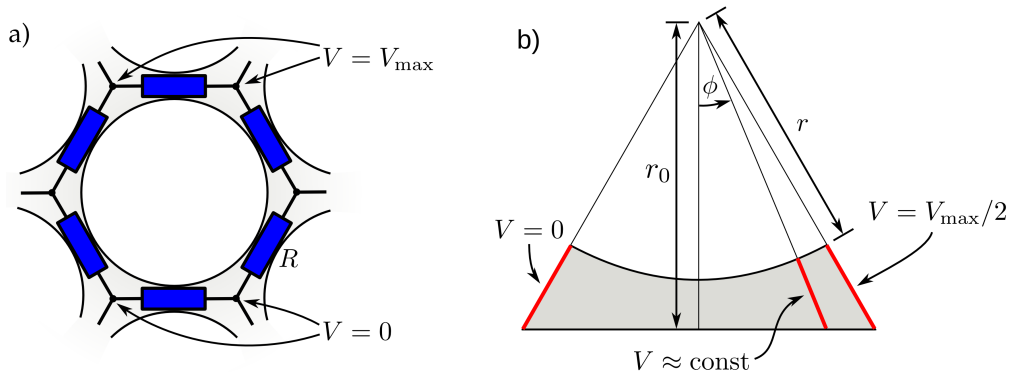


Fig. 9. Sketch of the lumped resistor configuration used in the analytical resistance model: a) The aperture-containing film is approximated as a network of lumped resistors. b) The value R of the lumped resistors is estimated under the assumption that the iso-voltage contours are straight lines towards the nearest aperture center. Panel b) also shows the relevant parameters of the geometry.

The problem reduces to solving for the electric potential inside half a vein under the condition of a constant current I . As an approximation, we assume that the isopotential contours are radial with respect to the nearest aperture center. The current through the contour associated with angle ϕ is:

$$\begin{aligned}
 I(\phi) &= 2\sigma_B t \frac{\partial V}{\partial \phi} \cdot \int_r^{r_0/\cos \phi} dr' \frac{1}{r'} \\
 &= 2\sigma_B t \frac{\partial V}{\partial \phi} \ln \left(\frac{r_0}{r \cos \phi} \right),
 \end{aligned}
 \tag{5}$$

where σ_B is the bulk conductivity of Ag. The factor 2 appears, because the integral only covers half the vein. Current is conserved, so the current through each isopotential contour is a constant parameter and we solve the equation for $(\partial V)/(\partial \phi)$, which we only have to integrate over the angle ϕ to obtain the voltage across one vein for a given current I :

$$\begin{aligned}
 \frac{1}{2}V_{\max} &= \int_{-\pi/6}^{\pi/6} d\phi \frac{\partial V}{\partial \phi} \\
 &= \frac{I}{\sigma_B t} \int_0^{\pi/6} d\phi \left[\ln \left(\frac{r_0}{r \cos \phi} \right) \right]^{-1} \\
 &\approx \frac{I}{\sigma_B t} \int_0^{\pi/6} d\phi \frac{1}{1 - a - \cos \phi},
 \end{aligned} \tag{6}$$

where we used the symmetry of the integrand, we introduced the parameter $a = \ln(r/r_0)$ and used the approximation $\ln(x) \approx x - 1$, which is accurate to about 1% for the range of ϕ in this integral. This integral has a closed solution:

$$\frac{1}{2}V_{\max} = \frac{I}{\sigma_B t} \frac{2}{\sqrt{a^2 - 2a}} \arctan \left(\frac{2 - a}{\sqrt{a^2 - 2a}} \cdot \tan \frac{\pi}{12} \right). \tag{7}$$

With an additional factor $\sqrt{3}/2$ correcting for the aspect ratio (the lumped resistive elements in the network have an angle of 120° relative to neighbor elements) of the film unit cell, we end up with Eq. (2) presented in the main text.

Funding

VILLUM FONDEN (16498); University of Southern Denmark (SDU 2020).

Acknowledgments

N. A. M. is a VILLUM Investigator supported by VILLUM FONDEN (grant No. 16498). Center for Nano Optics is financially supported by the University of Southern Denmark (SDU 2020 funding).

Disclosures

The authors declare that there are no conflicts of interest related to this article.